Available online at www.sciencedirect.com
ScienceDirect
Journal of Solid State Chemistry 180 (2007) 474–483
JOURNAL OF SOLID STATE CHEMISTRY
www.elsevier.com/locate/jssc

Structural and magnetic study of the cation-ordered perovskites $Ba_{2-x}Sr_xErMoO_6$

Edmund J. Cussen*

The School of Chemistry, The University of Nottingham, University Park, Nottingham NG7 2RD, UK

Received 27 September 2006; received in revised form 1 November 2006; accepted 4 November 2006
Available online 14 November 2006

Abstract

A series of perovskite phases have been prepared from the appropriate carbonates and oxides by heating under reducing conditions at temperatures up to 1300 °C. Complete ordering between ErO_6 and MoO_6 octahedra and a disordered distribution of Sr^{2+} and Ba^{2+} occur in all compounds. Neutron powder diffraction experiments show that the substitution of Sr^{2+} into Ba_2ErMoO_6 introduces a progressive reduction in symmetry from $Fm\bar{3}m$ ($x = 0$) to $I4/m$ ($x = 0.5$, 0.8) to $P2_1/n$ ($x = 1.25$, 1.75, 2.0). Magnetic susceptibility measurements indicate that all of these compounds show Curie–Weiss paramagnetism and that for $x < 1.25$ this behaviour persists down to 2 K. The monoclinically distorted compounds show magnetic transitions at low temperature and neutron diffraction has confirmed the presence of long-range antiferromagnetic order below 2.5 and 4 K in $Ba_{0.25}Sr_{1.75}ErMoO_6$ and Sr_2ErMoO_6, respectively. $Ba_{0.75}Sr_{1.25}ErMoO_6$, $Ba_{0.25}Sr_{1.75}ErMoO_6$ and Sr_2ErMoO_6 do not undergo structural distortion on cooling from room temperature.

Keywords: Perovskites; Magnetism; Metal oxides

1. Introduction

The flexibility of the perovskite structure permits the incorporation of a uniquely wide range of metals and oxidation states. This results in a diverse family of materials that show an array of interesting and potentially useful physical properties including magnetoresistance [1,2], metal-insulator transitions [3], ionic mobility [4,5] and ferromagnetism [6,7]. Incorporation of mixtures of elements and/or oxidation states can lead to phases with properties that could not be anticipated from the parent materials; $SrFeO_3$ is a metallic antiferromagnet [8], $SrMoO_3$ is a metallic conductor [9], but the mixed phase Sr_2FeMoO_6 is a half-metallic ferrimagnet [2] that shows room temperature magnetoresistance in modest magnetic fields due to almost complete chemical ordering of the Fe^{3+} and Mo^{5+} cations. An understanding of such complex electronic behaviour requires a detailed appreciation of the structure and in order to enhance our understanding of the structural chemistry of Mo^{5+}, we recently undertook a study [10] of Ba_2LnMoO_6 to probe the effects of changes in cation size on the structural and magnetic properties of cation-ordered perovskites.

Compounds from the series Ba_2LnMoO_6 were reported to be orthorhombic (La and Ce), tetragonal (Pr, Nd and Sm) and cubic (Eu–Lu) by Brandle and Steinfink [11] although structures were not reported. A recent structural and magnetic study [12] of Ba_2LnMoO_6 (Ln = Sm, Eu, Gd and Dy) concluded that all of these compounds crystallize with cubic symmetry ($Fm\bar{3}m$) and an ordered rock-salt arrangement of cations over the two crystallographic sites in this structure. Ba_2GdMoO_6 and Ba_2DyMoO_6 displayed Curie–Weiss paramagnetism with extremely weak antiferromagnetic interactions. The magnetic susceptibilities of Ba_2SmMoO_6 and Ba_2EuMoO_6 both pass through local, broad maxima at ca. 120 K which were assigned as transitions to antiferromagnetically ordered states [12]. We recently studied [10] these compounds as part of the series Ba_2LnMoO_6 (Ln = Nd, Sm, Eu, Gd, Dy, Ho, Er, Yb, Lu and Y) using both X-ray and neutron diffraction. The latter is invaluable in precisely determining the positions of the oxide anions and confirmed the assignment of cubic symmetry for Ba_2YMoO_6, Ba_2ErMoO_6 and

*Fax: +44 115 951 3563.
E-mail address: Edmund.Cussen@nottingham.ac.uk.

0022-4596/$ - see front matter © 2006 Elsevier Inc. All rights reserved.
doi:10.1016/j.jssc.2006.11.007

Ba_2YbMoO_6 and the presence of complete ordering of Ln and Mo in a rock salt arrangement. In such a cation-ordered cubic structure with antiferromagnetic interactions the magnetic behaviour can be determined by (i) the interaction between nearest neighbours e.g. the linear Ln^{3+}–O–Mo^{5+} pathway or (ii) the more numerous interaction between next-nearest neighbours of the same cation type e.g. the 90° pathway Mo^{5+}–O–O–Mo^{5+}. If (i) dominates, as in the magnetoresistive phase Sr_2FeMoO_6, then a ferrimagnetically ordered structure forms due to incomplete spin cancellation resulting from the antiparallel alignment of Fe^{3+} (d^5, $S=\frac{5}{2}$) and Mo^{5+} (d^1, $S=\frac{1}{2}$). However, if (ii) is the stronger interaction then perfect geometric frustration results [13]. Ba_2YMoO_6 contains a paramagnetic species (Mo^{5+}) on only one of the ordered cation sites and so the magnetic susceptibility measurements on this material provided a crucial insight into these cubic phases. Ba_2YMoO_6 remained paramagnetic to 2 K despite the strong antiferromagnetic interactions illustrated by the Weiss constant, $\Theta=-91(1)$ K [10]. Because of this, the absence of a maximum or divergence in the magnetic susceptibility for most compounds in the series was interpreted as indication of paramagnetism persisting to 2 K. The maxima observed for Ba_2SmMoO_6 and Ba_2EuMoO_6 were not taken as evidence of long-range antiferromagnetism due to the broad nature of the transitions, the temperature-dependence of the magnetic moment for Sm^{3+} and Eu^{3+} and the absence of hysteresis below the transition. Due to the high cross-sections for neutron absorption of Sm and Eu it is not straightforward to probe the low temperature structure via neutron diffraction to prove this point.

X-ray diffraction data clearly showed the presence of a tetragonal distortion at room temperature in Ba_2SmMoO_6 and Ba_2NdMoO_6 and this was confirmed for the latter by neutron diffraction data which identified the space group as $I4/m$. This distortion lifts the magnetic frustration associated with the cubic cation-ordered phases and this is further perturbed by the distortion to triclinic symmetry ($I\bar{1}$) observed on cooling the sample to 32 K. Examination of the geometry of the MoO_6 octahedron showed that this distortion was driven by Jahn Teller instability associated with the triply degenerate ground state of Mo^{5+} in octahedral coordination. At 15 K Ba_2NdMoO_6 forms a magnetically ordered phase containing antiferromagnetically coupled chains of ferromagnetically coupled cations. Consideration of this magnetic structure showed that the differing electronic populations of the orbitals in the t_{2g} manifold are responsible for the highly anisotropic exchange interactions implied by this unusual magnetic ground state.

This coupling of a Jahn Teller driven distortion with electronic behaviour suggests clear parallels between the behaviour of Mo^{5+} and the magnetoresistive manganates [6,14] and suggests that the presence of Mo^{5+} could lead to the development of unusual electronic phenomena. No other compounds in the series Ba_2LnMoO_6 showed any evidence of Jahn Teller instability and it was postulated that the room temperature tetragonal distortion of Ba_2NdMoO_6 is a key ingredient in predisposing the oxide sublattice to undergo the necessary displacements to provide electronic stabilization to the t_{2g}^1 ground state.

In order to test this hypothesis, and to see if the electronic instability of octahedrally coordinated Mo^{5+} can provide a general route to anisotropic magnetic exchange and novel electronic behaviour, we have prepared a series of compounds $Ba_{2-x}Sr_xErMoO_6$. The Ba_2ErMoO_6 end member forms a cubic phase [10] and our strategy involves introducing the Sr^{2+} cation in an attempt to provoke variable structural distortion in (mainly) the oxide sublattice to satisfy the bonding requirements of this smaller cation and recreate the distorted structure observed in Ba_2NdMoO_6. The low cross section to neutron absorption of erbium will permit the use of neutron diffraction to determine accurately the oxide anion displacements.

2. Experimental

Compounds of stoichiometry $Ba_{2-x}Sr_xErMoO_6$ were prepared under reducing conditions using standard solid-state techniques. Stoichiometric quantities of $BaCO_3$, $SrCO_3$, MoO_3 and Er_2O_3 (dried at 800 °C) were intimately mixed as powders and pressed into pellets of 13 mm diameter under a load of 1.5 tonnes. These were initially heated from 550 to 800 °C in air at a rate of 1 °C min^{-1} in order to minimize loss of molybdenum. The pellets were then ground and repelleted before being heated from 900 to 1250 °C at a rate of 1.5 °C min^{-1} under a flowing atmosphere of 5%H_2/95%N_2 and held at this temperature for 2 days. The samples were cooled to room temperature under this atmosphere, ground, repelleted and heated to 1250 °C for another 2 days. This process was repeated until the reaction was complete with an increase in temperature to 1300 °C for compositions where impurities remained after heating at 1250 °C for several days. The progress of the reaction was monitored using X-ray powder diffraction and was judged to be complete when the product yielded a diffraction pattern which could be indexed as a single phase.

X-ray powder diffraction data were collected using a Philips Xpert powder diffractometer operating with Cu K_α radiation in Bragg Brentano geometry. Data were collected over the range $10\leqslant 2\theta\leqslant 90$ using a step size of $\Delta 2\theta=0.02°$ from samples mounted on an aluminium slide. Neutron powder diffraction data were collected using the constant wavelength instrument D2B at the Institut–Laue Langevin, Grenoble over the angular range $10\leqslant 2\theta\leqslant 155$ with a step size of $\Delta 2\theta=0.05°$. The samples were contained in cylindrical vanadium cans of internal diameters between 7 and 12 mm in order to give fill depths of 20–30 mm. The diffraction data were analysed by Rietveld refinement [15] using the GSAS suite of programs [16]. The background was modelled using a shifted Chebyshev function and the

Bragg peak shape was modelled using a pseudo–Voigt function. The magnetic form factor for Er^{3+} was described using literature values [17]. No form factor was available for the Mo^{5+} cation and so the form factor for Mn^{3+} was employed instead due to the similarities in the radii of the two cations.

Magnetic measurements were carried out using a Quantum Design SQUID magnetometer. The samples were contained in gelatine capsules which were themselves mounted in straws to provide an invariant diamagnetic background that did not influence the SQUID detection coils. DC susceptibility measurements were carried out in applied fields of 100 and 1000 G after cooling the sample in either zero applied field (zfc) or the measuring field (fc).

3. Results

The end member Ba_2ErMoO_6 has been shown to adopt a cation-ordered perovskite with cubic symmetry, $Fm\bar{3}m$ [10]. X-ray powder diffraction data collected from the sample containing the greatest concentration of Ba^{2+} provided no obvious evidence of a distortion from this symmetry, but close examination of Bragg peaks $2\theta > 70^\circ$ showed a small, unresolved splitting of the reflections which was incompatible with cubic symmetry but could be modelled using a tetragonal cell with lattice parameters $a \approx (a_p/\sqrt{2})$ and $c = 2a_p$ where a_p is the lattice parameter of the primitive cubic perovskite. The reduction in symmetry was more obvious in the neutron diffraction data which contain additional Bragg peaks which are systematically absent in the higher symmetry cell. Tetragonal distortions from cubic symmetry can be described in either of the space groups $I4/mmm$ or $I4/m$ [18]. The former allows an apical adjustment of the metal oxide octahedra along the four-fold axis whilst the latter additionally permits a rotation of the octahedra about this axis. Attempts to fit the neutron diffraction data in both of these space groups showed that the lower symmetry description was necessary to provide a reasonable intensity match to the additional peaks and so the data were fitted in $I4/m$ with a small quantity (1.8(1) wt%) or Er_2O_3 impurity. The refinement rapidly converged to give a good match with the observed diffraction profile. The data collected from $Ba_{1.2}Sr_{0.8}ErMoO_6$ were modelled in the same way to give a similar quality of fit as shown in Fig. 1. This structural distortion can be described in the Glazer notation as $a^0a^0c^-$ indicating an out-of-phase rotation about one axis such that neighbouring Mo/ErO_6 octahedra are rotated in opposite senses. Different tilting modes $a^0a^0c^+$ and $a^0b^-b^-$ are described in the space groups $P4/mnc$ and $I2/m$, respectively, and in order to test the robustness of the $I4/m$ fit, additional refinements were undertaken in both of these spacegroups. In the tetragonal space group $P4/mmc$ the refinement converged to give an unacceptably poor quality of fit ($R_{wp} = 8.56$, $\chi^2 = 19.4$). The space group $I2/m$ is an unconventional setting of the monoclinic space group $C2/m$ and in this case the refined structural model provided a degraded fit to the structure

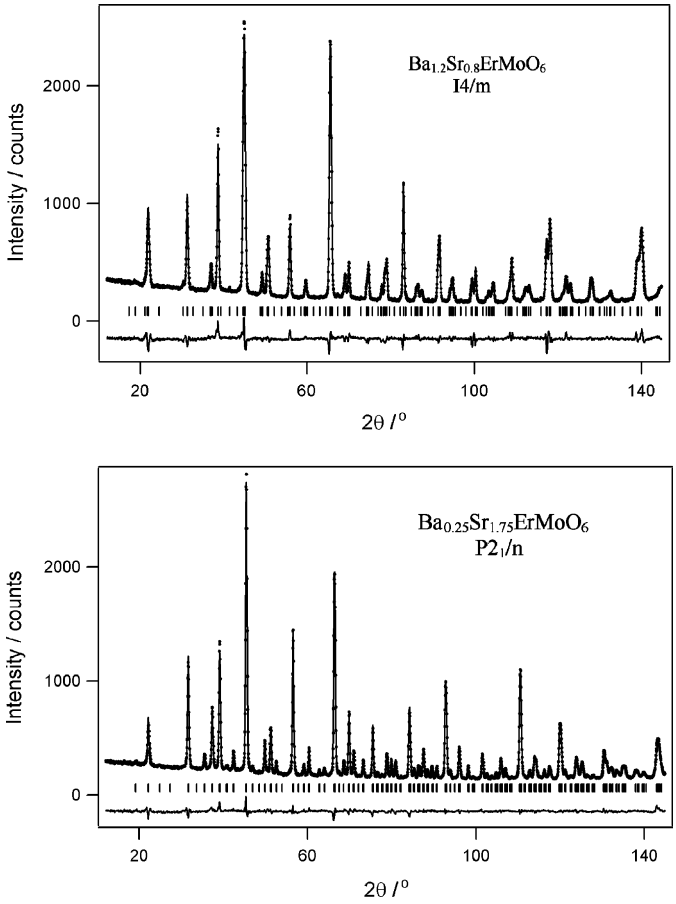

Fig. 1. Observed (dots), calculated (line) and difference neutron diffraction profiles collected from $Ba_{1.2}Sr_{0.8}ErMoO_6$ and $Ba_{0.25}Sr_{1.75}ErMoO_6$ at room temperature.

($R_{wp} = 5.03$, $\chi^2 = 6.714$) and did not converge without damping of the atomic positions and the lattice parameters due to correlation in both of these variables. Attempts to fit the data using the space group $P2_1/n$ ($a^-a^-c^+$) were similarly unsatisfactory ($R_{wp} = 5.18$, $\chi^2 = 7.13$). These fits to monoclinic symmetry are both slightly but significantly worse than that obtained in the tetragonal spacegroup $I4/m$ ($R_{wp} = 4.79$, $\chi^2 = 6.06$) despite the increased number of variable atomic positions and suggest that the $a^0a^0c^-$ tilt system described in this tetragonal space group provides the correct description of the structural distortion in $Ba_{1.2}Sr_{0.8}ErMoO_6$.

The neutron diffraction data collected from $Ba_{0.75}Sr_{1.25}ErMoO_6$ showed peak broadening at high angle and the presence of weak Bragg peaks which were systematically absent in the $I4/m$ cell, but both of these features were accurately modelled by a reduction in symmetry to $P2_1/n$ in a cell of approximately the same dimensions as $I4/m$. The structures of $Ba_{0.25}Sr_{1.75}ErMoO_6$ and Sr_2ErMoO_6 were also modelled in this monoclinic space group. The evolution of structure with increasing strontium content is illustrated in Fig. 2. Trial refinements using an anisotropic description of the displacement parameters

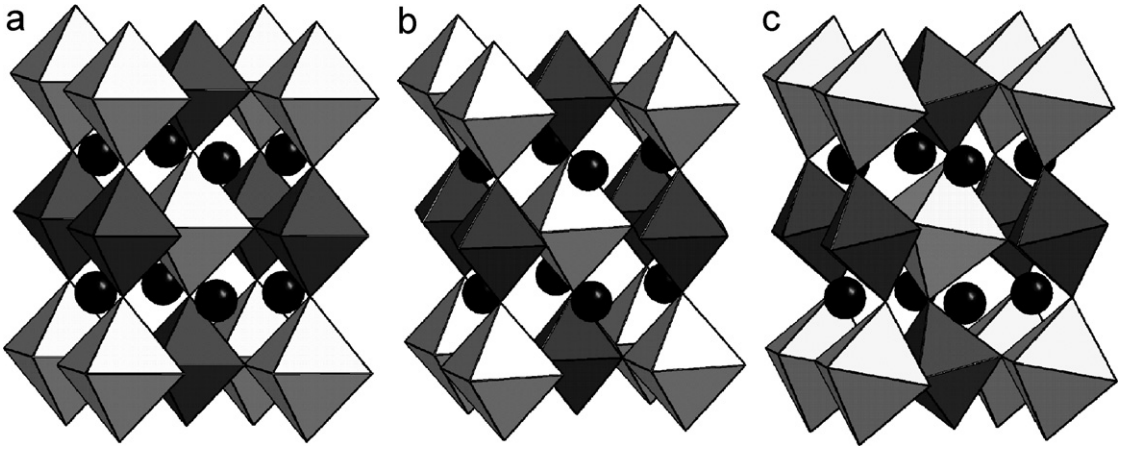

Fig. 2. The room temperature structures of (a) cubic Ba_2ErMoO_6, (b) tetragonal $Ba_{1.2}Sr_{0.8}ErMoO_6$ and (c) monoclinic Sr_2ErMoO_6. Dark and light grey octahedra represent MoO_6 and ErO_6 units respectively and Sr^{2+}/Ba^{2+} cations are shown as black spheres.

Table 1
Fit parameters and structural information derived from fitting the neutron diffraction data collected from $Ba_{2-x}Sr_xErMoO_6$ at room temperature unless otherwise stated

	$I4/m$[a]		$P2_1/n$[b]					
x	0.50	0.80	1.25	*1.25 (1.6 K)*	1.75	*1.75 (1.6 K)*	2.00	*2.00 (4 K)*
a (Å)	5.89879(16)	5.86453(9)	5.86691(13)	*5.85593(13)*	5.81211(14)	*5.8007(2)*	5.78711(16)	*5.7724(2)*
b (Å)	5.89879	5.86453	5.8491(10)	*5.84293(11)*	5.8176(13)	*5.8185(2)*	5.80692(13)	*5.81388(12)*
c (Å)	8.3262(5)	8.3457(2)	8.2456(2)	*8.2273(2)*	8.2111(2)	*8.1895(2)*	8.1900(2)	*8.1603(2)*
β (°)	90	90	90.144(2)	*90.182(2)*	90.177(2)	*90.227(2)*	90.202(2)	*90.296(1)*
R_{wp}	4.88	4.79	3.92	*3.41*	3.39	*3.69*	2.60	*2.48*
χ^2	6.40	6.06	3.40	*1.956*	2.73	*2.12*	2.38	*2.52*
Ba/Sr x	0	0	0.0048(6)	*0.0047(6)*	0.0055(7)	*0.0052(8)*	0.0050(6)	*0.0070(5)*
Ba/Sr y	$\frac{1}{2}$	$\frac{1}{2}$	0.0058(9)	*0.0146(5)*	0.0227(3)	*0.0284(3)*	0.0282(3)	*0.0339(2)*
Ba/Sr z	$\frac{1}{4}$	$\frac{1}{4}$	0.2477(7)	*0.2476(6)*	0.2476(6)	*0.2497(7)*	0.2473(6)	*0.2495(4)*
Ba/Sr U_{iso} (Å^2)	0.0119(3)	0.0135(3)	0.0128(3)	*0.0049(3)*	0.0141(3)	*0.0065(3)*	0.0109(3)	*0.0044(3)*
Er/Mo U_{iso} (Å^2)	0.0090(3)	0.0084(2)	0.0057(2)	*0.0026(2)*	0.0073(2)	*0.0058(2)*	0.0058(2)	*0.0038(2)*
O(1) x	0.2426(7)	0.2346(4)	0.2535(7)	*0.2585(6)*	0.2674(6)	*0.2696(7)*	0.2705(7)	*0.2705(4)*
O(1) y	0.2799(6)	0.2902(4)	0.2711(10	*0.2813(8)*	0.2915(6)	*0.2963(7)*	0.2954(6)	*0.3009(4)*
O(1) z	0	0	0.0257(7)	*0.0292(6)*	0.0322(5)	*0.0346(6)*	0.0342(5)	*0.0370(4)*
O(1) U_{iso} (Å^2)	0.0260(8)	0.0213(4)	0.0193(12)	*0.0139(9)*	0.0149(9)	*0.0093(10)*	0.0157(8)	*0.0087(7)*
O(2) x	0	0	0.2831(8)	*0.2864(6)*	0.2976(6)	*0.2969(7)*	0.3027(6)	*0.3019(4)*
O(2) y	0	0	0.2589(10)	*0.2598(7)*	0.2688(7)	*0.2677(8)*	0.2742(8)	*0.2734(5)*
O(2) z	0.2667(5)	0.2645(4)	0.4686(7)	*0.4671(5)*	0.4643(5)	*0.4620(5)*	0.4616(4)	*0.4586(3)*
O(2) U_{iso} (Å^2)	0.0069(9)	0.0206(7)	0.0175(13)	*0.0048(8)*	0.0168(8)	*0.0093(9)*	0.0101(6)	*0.0056(5)*
O(3) x	—	—	0.9430(5)	*0.9398(4)*	0.9339(6)	*0.9305(6)*	0.9289(6)	*0.9267(3)*
O(3) y	—	—	0.4959(11)	*0.4925(7)*	0.4885(6)	*0.4874(6)*	0.4857(6)	*0.4833(3)*
O(3) z	—	—	0.2348(4)	*0.2357(4)*	0.2368(4)	*0.2361(5)*	0.2382(4)	*0.2353(3)*
O(3) U_{iso} (Å^2)	—	—	0.0128(7)	*0.0096(6)*	0.0163(6)	*0.0107(7)*	0.0116(5)	*0.0068(4)*

[a]Contains Mo on 2*b* (0, 0, $\frac{1}{2}$) and Er on 2*a* (0, 0, 0).
[b]Contains Mo on 2*d* (0, $\frac{1}{2}$, 0) and Er on 2*a* ($\frac{1}{2}$, 0, 0).

gave no significant improvement in the quality of the fit and led to large correlations between these variables. Refinements were attempted in which the oxide site occupancy and the Er/Mo distribution were allowed to vary in order to model anion non-stoichiometry and octahedral site disorder respectively. These indicated that there was negligible departure from unity for either of these parameters. In the final models the oxide sites occupancies were set at unity, the Er/Mo distribution was fixed to model perfect ordering and the temperature factors were described isotropically. The resulting quality of fit indices, lattice parameters and atomic coordinates are collected in Table 1 and the significant interatomic distances and angles are listed in Table 2.

3.1. Magnetic measurements

All compounds showed paramagnetic behaviour at high temperatures as illustrated in Fig. 3. Magnetic susceptibility data were fitted over the temperature range

Table 2
Interatomic distances (Å) and angles (°) derived from fitting the neutron diffraction data collected from $Ba_{2-x}Sr_xErMoO_6$ at room temperature

	$I4/m$		$P2_1/n$		
	$x = 0.5$	$x = 0.80$	$x = 1.25$	$x = 1.75$	$x = 2.00$
A–O(1)	2.840(2) × 4	2.7860(11) × 4	2.715(7)	2.609(6)	2.589(6)
A–O(1)	3.060(2) × 4	3.1096(12) × 4	2.811(9)	2.814(6)	2.799(6)
A–O(1)	—	—	3.025(8)	2.925(6)	2.904(6)
A–O(1)	—	—	3.160(7)	3.334(6)	3.370(6)
A–O(2)	2.9527(2) × 4	2.93478(12) × 4	2.612(8)	2.557(6)	2.521(6)
A–O(2)	—	—	2.857(8)	2.842(5)	2.840(6)
A–O(2)	—	—	2.978(9)	2.886(6)	2.854(7)
A–O(2)	—	—	3.278(7)	3.405(6)	3.459(6)
A–O(3)	—	—	2.632(5)	2.564(6)	2.526(6)
A–O(3)	—	—	2.891(8)	2.743(4)	2.694(3)
A–O(3)	—	—	3.006(8)	3.137(4)	3.181(3)
A–O(3)	—	—	3.243(5)	3.267(6)	3.287(4)
Mo–O(1)–Er	180	180	167.0(3)	160.2(2)	158.5(2)
Mo–O(2)–Er	171.4(1)	167.31(9)	162.8(3)	157.8(2)	155.4(2)
Mo–O(1)	1.998(4) × 4	1.984(3) × 4	2.012(5) × 2	1.988(3) × 2	1.984(4) × 2
Mo–O(2)	1.942(4) × 2	1.965(4) × 2	1.995(5) × 2	1.978(4) × 2	1.984(3) × 2
Mo–O(3)	—	—	1.966(4) × 2	1.985(3) × 2	1.997(3) × 2
Er–O(1)	2.185(4) × 4	2.189(3) × 4	2.157(5) × 2	2.187(3) × 2	2.188(3) × 2
Er–O(2)	2.221(4) × 2	2.207(4) × 2	2.195(4) × 2	2.211(4) × 2	2.212(3) × 2
Er–O(3)	—	—	2.212(4) × 2	2.194(3) × 2	2.183(3) × 2
O(1)–Mo–O(2)	90	90	88.84(3)	89.9(2)	89.7(2)
O(1)–Mo–O(3)	—	—	89.1(2)	89.8(2)	89.8(2)
O(2)–Mo–O(3)	—	—	89.5(3)	89.8(2)	89.93(13)
O(1)–Er–O(2)	90	90	87.3(3)	88.4(2)	88.0(2)
O(1)–Er–O(3)	—	—	89.4(3)	89.4(14)	89.04(12)
O(2)–Er–O(3)	—	—	89.4(2)	89.18(14)	89.10(14)
Mo–O(3)–Er	—	—	161.5(2)	158.4(2)	156.8(2)

$50 \leqslant T$ (K) $\leqslant 300$ using the Curie–Weiss law. In this paramagnetic regime the data showed no dependence on the size of the applied magnetic field and the fitted values for the Weiss constants and Curie constants as well as the moments derived from the latter are collected in Table 3. The data collected from $Ba_{1.50}Sr_{0.50}ErMoO_6$ and $Ba_{1.20}Sr_{0.80}ErMoO_6$ showed no evidence of divergence between field cooled (fc) and zero field cooled (zfc) data over the whole temperature range. However the strontium-rich phases showed history dependence and at low temperatures a clear field dependence was observed in these compounds. The data collected from $Ba_{0.25}Sr_{1.75}ErMoO_6$ and Sr_2ErMoO_6 showed divergence between zfc and fc data and a maximum in the zero field cooled susceptibility at 2.5 and 4 K, respectively, when a field of 100 G was applied as shown in Figs. 4 and 5. No maximum was observed in the data collected from $Ba_{0.75}Sr_{1.25}ErMoO_6$ but divergence was shown below 2.5 K in a field of 100 G. When all of these measurements were repeated in an applied field of 1000 G neither the maxima in the zfc data nor the divergence between zfc and fc data were observed as shown for Sr_2ErMoO_6 in Fig. 5. This field dependence was tested over multiple data collections using several different samples for each of these compositions. In all cases the observed behaviour was exactly reproduced showing that the effect is an intrinsic property of these compounds.

3.2. Low T neutron diffraction data

Neutron diffraction data collected from $Ba_{0.75}Sr_{1.25}ErMoO_6$ at 1.6 K were readily modelled using a refinement of the room temperature, monoclinic structure. Data were collected from $Ba_{0.25}Sr_{1.75}ErMoO_6$ at both 1.6 and 4 K, i.e. below and above the maximum observed in the zfc magnetic susceptibility. The diffraction pattern collected at 1.6 K was similar to that observed at room temperature and so these data were fitted using the monoclinic structure as a starting model. This provided a good fit to the majority of the patterns but provided a poor match to some of the weak peaks observed at low angle. Due to the poor resolution in d-spacing at low diffraction angles and the closeness of the metric unit cell to tetragonally symmetry it was not possible to differentiate between the contributions of (hkl), (khl), $(\bar{h}kl)$ and $(h\bar{k}l)$ to a single observed diffraction peak. The intensities of the $(111)/(1\bar{1}1)$ and $(102)/(10\bar{2})$ reflections were significantly underestimated by the nuclear model and an additional Bragg peak was observed which could be indexed as the (100) or (010) reflections of a unit cell of the same dimensions, i.e. it violated the extinction conditions associated with the space group $P2_1/n$. The neutron diffraction data collected at 4 K did not contain any of these low-angle features and consequently could be satisfactorily fitted using a

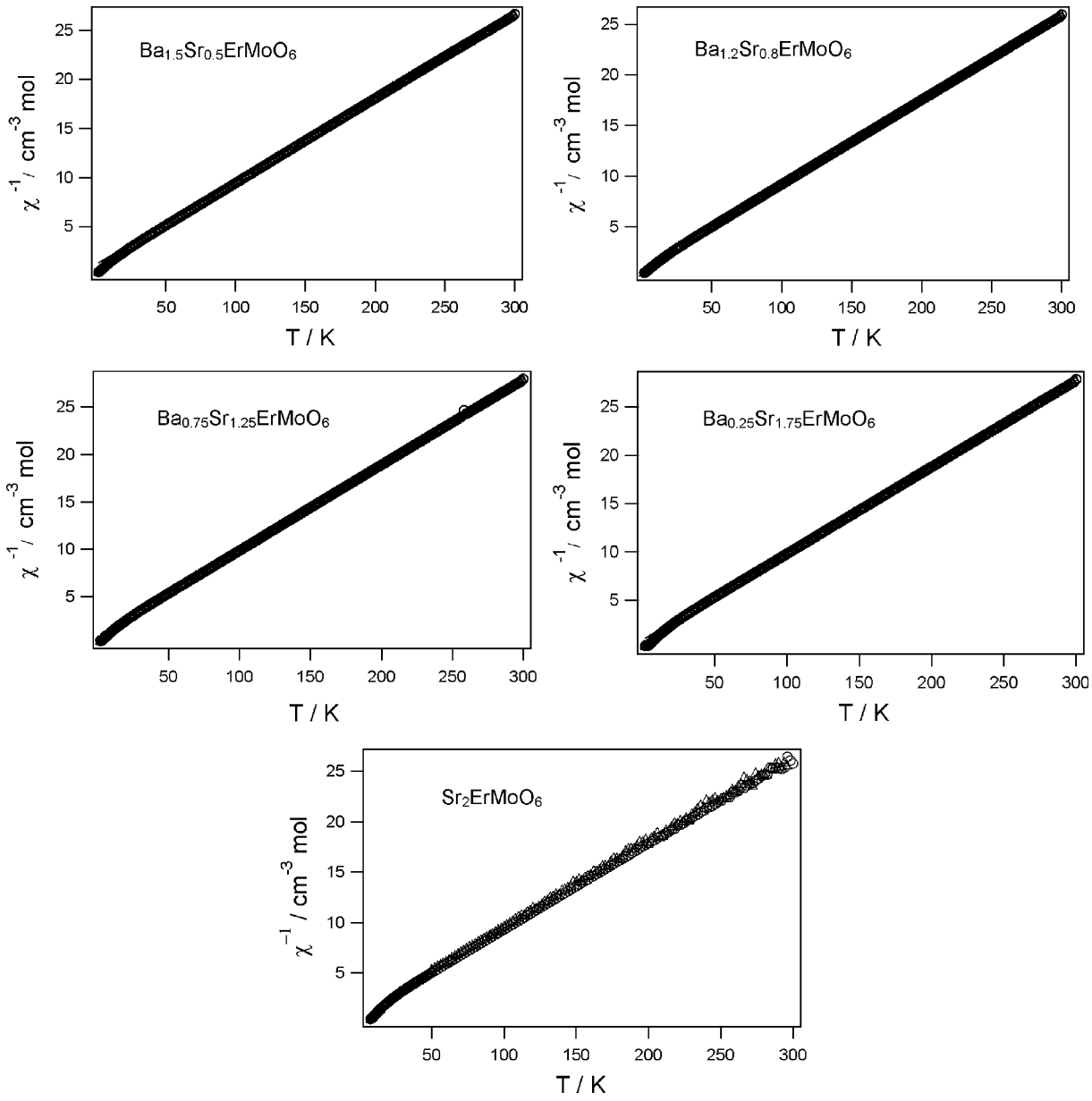

Fig. 3. Inverse molar magnetic susceptibilities of $Ba_{2-x}Sr_xErMoO_6$ recorded in an applied field of 100 G. Data collected after cooling in zero applied field (circles) or the measuring field (triangles) overlie one another.

Table 3
The magnetic parameters derived from fitting magnetic susceptibility data to the Curie–Weiss law in the range $50 \leqslant T\,(\mathrm{K}) \leqslant 300$

x	0.50	0.80	1.25	1.75	2.00
C ($\mathrm{cm^3\,K\,mol^{-1}}$)	11.615(2)	12.943(2)	11.086(2)	11.156(1)	11.68(1)
θ (K)	−9.45(2)	−9.70(2)	−9.27(2)	−9.443(8)	−8.71(8)
$\mu_{\mathrm{eff}}/\mu_{\mathrm{B}}$	9.64	10.18	9.42	9.45	9.67
T_{N} (K)				2.5	4.0

straightforward refinement of the room temperature structure. The disappearance of these Bragg peaks on heating the sample through the magnetic transition temperature suggests that the additional observed intensity is due to long-range magnetic ordering of the magnetic moments in $Ba_{0.25}Sr_{1.75}ErMoO_6$. The maximum in the zfc magnetic susceptibility of this compound indicates that the magnetically ordered structure must lead to spin cancellation, i.e. the magnetic Bragg peaks are associated with the formation of an antiferromagnetically ordered phase. The magnetic peaks could be indexed in a unit cell of the same dimensions as the nuclear cell (i.e. $\mathbf{k} = [000]$) and so trial refinements employed a model which contained two Er^{3+} in the unit cell which were constrained to align antiparallel to one another. An excellent quality of fit to the data was achieved in which the magnetic moment were ordered along either the x or y directions of the nuclear cell with a

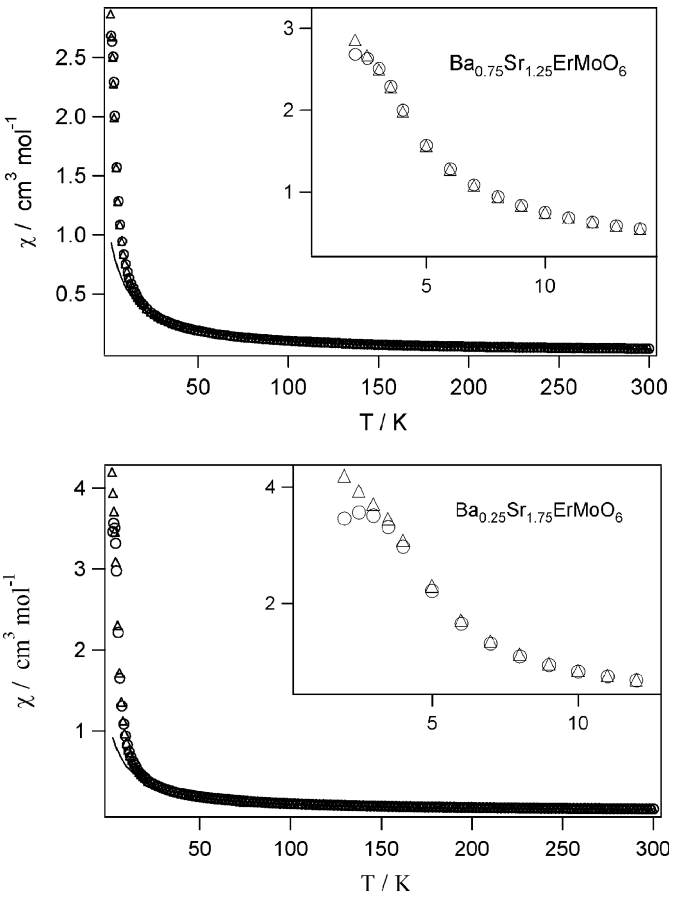

Fig. 4. Magnetic susceptibilities of $Ba_{0.75}Sr_{1.25}ErMoO_6$ and $Ba_{0.25}Sr_{1.75}ErMoO_6$ recorded after cooling the sample in zero applied field (circles) or after cooling in the applied measuring field of 100 G (triangles). The Curie–Weiss fit is shown by a solid line in each case.

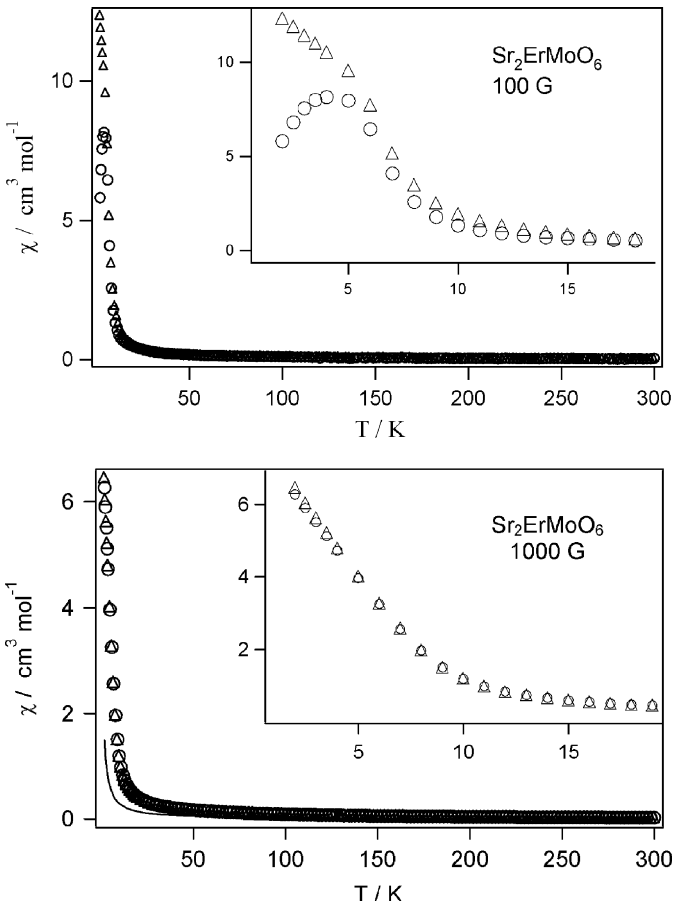

Fig. 5. Magnetic susceptibility of Sr_2ErMoO_6 recorded in an applied field of 100 G (top) and 1000 G (bottom). Data were recorded after cooling the sample in zero applied field (circles) and after cooling in the measuring field (triangles) and the Curie–Weiss fit is shown by a solid line.

refined magnetic moment of 2.20(10) μ_B per Er^{3+}. The fitted diffraction pattern is shown in Fig. 6.

Alternative refinements with the moments along z significantly degraded the quality of the fit and modelling the magnetic scattering as arising from ordering of Mo^{5+} made a negligible change to the value of the refined moment. An accurate model of the observed magnetic scattering was thus achieved using a single antiferromagnetically ordered moment constrained along either [100] or [010] directions. Due to the limited number of Bragg peaks, the closeness of the unit cell to higher metric symmetry and the proximity to the Néel temperature this model is necessarily a simplification. However, the crude conclusion of an ordered moment of ca. 2 μ_B is a robust one. The data collected from Sr_2ErMoO_6 at 3.5 K, i.e. below the magnetic transition at 4 K, were fitted using the room temperature structure as a starting point for the refinement and the same magnetic structure as that determined for $Ba_{0.25}Sr_{1.75}ErMoO_6$. This provided a good match to the observed data and resulted in a refined magnetic moment of 1.97(6) μ_B per Er^{3+} cation.

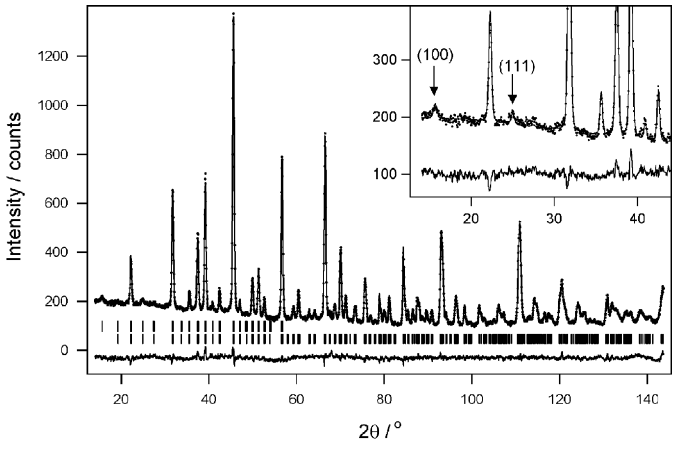

Fig. 6. Observed (dots), calculated (line) and difference neutron diffraction pattern collected from $Ba_{0.25}Sr_{1.75}ErMoO_6$ at 1.6 K. The upper and lower tick marks indicate allowed Bragg peaks associated with the magnetic and nuclear cells respectively. The inset shows the low angle region containing the magnetic contribution to the (100) and (111) peaks which show no detectable intensity in an additional dataset collected at 4 K.

4. Discussion

4.1. Structure

The title compounds form a series of double perovskites containing Er^{3+} and Mo^{5+} in a perfectly ordered rock salt arrangement over the two octahedrally coordinated sites in the crystal structure. Both the ErO_6 and MoO_6 octahedra are highly regular and the latter exhibit Mo–O bond lengths, ca. 1.97 Å, typical for Mo^{5+} in octahedral coordination [10,19,20]. The introduction of strontium induces structural distortions from the cubic structure which increase with Sr^{2+} concentration. Such distortions are a well-understood feature of the perovskite structure and are driven by a size mismatch between the central interstitial site and the radius of the coordinated cation. This is clearly illustrated by the Sr/Ba–O bond lengths and coordination numbers in $Ba_{2-x}Sr_xErMoO_6$. For $x = 0.50$ and 0.80 the alkaline earth cations show the same twelve coordination as the cubic end member Ba_2ErMoO_6; but with increasing strontium content this is progressively reduced to nine-coordination in the end-member Sr_2ErMoO_6. The observed structural evolution from $Fm\bar{3}m$ to $I4/m$ to $P2_1/n$ is in agreement with predictions based on symmetry considerations [18]. It also shows that reducing the size of the alkaline earth cation gives access to structural distortions that are similar to those obtained by increasing the lanthanide size in Ba_2LnMoO_6, i.e. the tetragonal phases observed for Ln = Nd, Sm. Whilst the distortion of the individual MO_6 units in $Ba_{2-x}Sr_xErMoO_6$ is minimal, the mean Mo–O–Er angle between the octahedra evolves smoothly as the mean size of the A cation is reduced as shown in Fig. 7.

In the tetragonally distorted compounds one of these angles is constrained by symmetry to be linear whilst the other two linkages are free to move in the xy plane. Increasing the strontium content beyond $x = 0.8$ reduces the symmetry thus removing constraints on the Mo–O–Er angles linking the octahedra so that three independent values occur. It is interesting to note that in monoclinic symmetry the third Mo–O–Er angle perpendicular to this plane deviates from linearity rapidly as a function of stoichiometry such that for $Ba_{0.25}Sr_{1.75}ErMoO_6$ and Sr_2ErMoO_6 all the three angles take very similar values of 159° and 157°, respectively. The isotropic displacement parameters show some variation with composition taking the largest values around $x = 1$ where the degree of chemical disorder between Sr^{2+} and Ba^{2+} is maximized. This observation is consistent with a considerable static contribution to the positional disorder due to the random occupancy of sites with either Sr^{2+} or Ba^{2+} and the associated local variation in alkaline earth metal–oxide bond lengths.

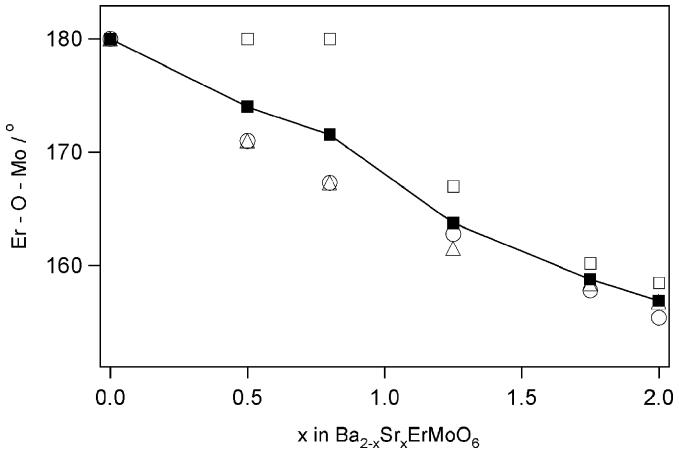

Fig. 7. Variation in Er–O–Mo angle as a function of composition in the series $Ba_{2-x}Sr_xErMoO_6$. The solid symbols indicate the mean angle. Value for Ba_2ErMoO_6 are taken from [10] and the errors associated with the values are substantially smaller than the symbols used.

The structural refinements of $Ba_{0.75}Sr_{1.25}ErMoO_6$, $Ba_{0.25}Sr_{1.75}ErMoO_6$ and Sr_2ErMoO_6 at $T \leqslant 4$ K show that no significant changes in structure occur on cooling beyond a slight increase in the metric distortion; it is particularly noteworthy that the MoO_6 octahedra remain largely regular with Mo–O bond lengths in the range 1.972(3)–1.985(4) for $Ba_{0.75}Sr_{1.25}ErMoO_6$; 1.973(4)–1.981(3) Å for $Ba_{0.25}Sr_{1.75}ErMoO_6$ and 1.966(2)–1.987(2) Å Sr_2ErMoO_6. These can be contrasted with the molybdenum environment in Ba_2NdMoO_6 at 3.5 K which gives pairs of Mo–O bond lengths 1.956(7), 1.959(8) and 2.023(3) Å [10].

4.2. Magnetic properties

All compounds show paramagnetic behaviour at all except the lowest temperatures accessed. In every case the observed paramagnetic magnetic moment shows reasonable agreement with the value ($9.73\,\mu_B$) calculated on the basis of a spin-only contribution from Mo^{5+} and the fully coupled orbital and spin contribution associated with the $^4I_{15/2}$ state of Er^{3+}. The Weiss constant for this series of compounds shows only a small variation in the range $-10.0 < |\theta|\,(K) < -13.7$ indicating that all materials contain weak antiferromagnetic interactions similar to those observed in Ba_2ErMoO_6 ($\theta = -9.5(2)$ K). This provides an estimate of the mean interaction between paramagnetic centres in these phases and gives an indication of the maximum possible value of the magnetic ordering temperature. The strength of magnetic superexchange is rapidly diminished by reduction in orbital overlap along the exchange path and so the strongest magnetic coupling could be anticipated to occur when the Mo–O–Er angles are closest to linear. However, it is well known that a face-centred cubic lattice exhibits perfect geometric frustration [13] and thus is not anticipated to exhibit a magnetically ordered ground state. Studies of Ba_2ErMoO_6 have shown that this is the case with paramagnetism persisting down to at least 2 K [10]. All of the compositions in the present study display either tetragonal or monoclinic distortions from face-centred cubic symmetry that remove the three-dimensional equivalence of the magnetic exchange between

the metal oxide octahedra. Consequently, these structural distortions reduce the strength of individual magnetic exchange interactions, but increase the net interaction due to the lifting of frustration.

Magnetic susceptibility measurements indicate that both tetragonal compounds remain paramagnetic down to 2 K. The monoclinic phase $Ba_{0.75}Sr_{1.25}ErMoO_6$ shows divergence in the magnetic susceptibility data at the lowest temperatures accessed. On increasing the Sr^{2+} content further, a clear maximum is observed in the zfc data at 2.5 and 4.0 K for $Ba_{0.25}Sr_{1.75}ErMoO_6$ and Sr_2ErMoO_6 respectively. Low temperature neutron diffraction data collected from both of these compounds contain Bragg peaks due to magnetic ordering and confirm the presence of antiferromagnetism. Due to the proximity of the Néel temperatures to the conditions of data collection, it is to be expected that the observed ordered magnetic moments are reduced from that expected for Er^{3+} ($gJ = (1.2 \times 15/2) = 9\,\mu_B$) but the observed moments are larger than that associated with complete ordering of Mo^{5+} ($gS = 1\,\mu_B$) and so provide clear evidence of the presence of antiferromagnetic ordering of the Er^{3+} sublattice. Due to the small amount of magnetic Bragg scattering from these phases the magnetic model is underdetermined and therefore a more detailed analysis of the magnetic structure is not merited. Because of the population of the 4d orbitals the magnetic interactions of Mo^{5+} are stronger than Er^{3+} and could lead to the Mo–O–O–Mo interaction between next nearest neighbours dominating over the shorter Mo–O–Er interaction. However, the magnetic susceptibility measurements showed no evidence of magnetic order above the antiferromagnetic transition temperatures identified by neutron diffraction and so we conclude that both Mo^{5+} and Er^{3+} are paramagnetic at elevated temperatures and undergo simultaneous antiferromagnetic ordering at the temperatures indicated by maxima in the zfc susceptibility data. We note that the higher magnetic ordering temperatures of the monoclinically distorted perovskites Ba_2PrRuO_6 [21], Sr_2ErRuO_6 [22], Sr_2HoRuO_6 [23], and Sr_2TbRuO_6 [23] have permitted more detailed studies of magnetic structures in these closely related phases. The simultaneous ordering of the magnetic moments of Ln^{3+} and Ru^{5+} in these compounds provides some support for the assignment of a single magnetic transition in the compounds presently under discussion.

It is interesting to note that for $Ba_{2-x}Sr_xErMoO_6$ the Néel temperatures evolve incrementally as a function of Sr-content and are all significantly lower than that observed in Ba_2NdMoO_6 ($T_N = 15$ K). Presumably the enhancement in ordering temperature in Ba_2NdMoO_6 arises from the anisotropic magnetic exchange interaction associated with the Jahn Teller distortion of Mo^{5+}. The presence of chemical disorder on the *A* site of the perovskite structure could impede the propagation of subtle structural distortions. However, the straightforward trend in structural evolution and antiferromagnetic ordering temperatures for $Ba_{0.75}Sr_{1.25}ErMoO_6$, $Ba_{0.25}Sr_{1.75}ErMoO_6$ and Sr_2ErMoO_6 suggest that the presence of Ba/Sr disorder does not have a substantial role in this system. Given that the electronic stabilization energy afforded by a structural distortion would be the same in all Mo^{5+} compounds, the observation of largely regular MoO_6 octahedra for all compounds in the series $Ba_{2-x}Sr_xErMoO_6$ is unexpected. The interactions of the Nd^{3+}, Er^{3+}, Ba^{2+} and Sr^{2+} cations are all anticipated to be largely ionic, and hence isotropic, and so would not introduce conditions to favour particular structural distortions. However, the observation of a regular Mo^{5+} environment across a variety of distorted double perovskite in the $Ba_{2-x}Sr_xErMoO_6$ system suggests that there is some characteristic of the Ba_2NdMoO_6 framework which renders it peculiarly amenable to such a distortion.

5. Conclusions

The compounds $Ba_{2-x}Sr_xErMoO_6$ form a pseudo solid-solution of cation-ordered perovskites. The introduction of Sr^{2+} is responsible for increasingly large distortions from cubic symmetry and these can be rationalized using geometric considerations. The ErO_6 and MoO_6 units are perfectly ordered in a rock salt arrangement and, despite the various tilting modes introduced to accommodate Sr^{2+} in the structure, these octahedra remain highly regular. Magnetic interactions between the moments of Er^{3+} and Mo^{5+} are extremely weak in all compounds; antiferromagnetic order is only observed in the most distorted phases and the Néel temperature reaches a maximum value of only 4 K. These compounds thus show wholly different magnetic behaviour to the Jahn Teller distorted phase Ba_2NdMoO_6 that undergoes an antiferromagnetic transition at 15 K. It may be that the structure of Ba_2NdMoO_6 happens to be exactly optimized to encourage the formation of a distorted metal coordination environment and that the conditions for Jahn Teller activity of Mo^{5+} require more careful adjustment than has been afforded in the $Ba_{2-x}Sr_xErMoO_6$ system.

Acknowledgments

This work was supported by the Royal Society by the provision of a University Research Fellowship and a Research Grant. Dr Cussen is grateful to Dr Clemens Ritter and Dr Paul Henry at the Institut–Laue Langevin, Grenoble for experimental assistance with neutron diffraction experiments and to the EPSRC for providing access to this facility.

References

[1] N.D. Mathur, G. Burnell, S.P. Isaac, T.J. Jackson, B.S. Teo, J.L. MacManus-Driscoll, L.F. Cohen, J.E. Evetts, M.G. Blamire, Nature 387 (1997) 266.

[2] K.-I. Kobayashi, T. Kimura, H. Sawada, K. Terakura, Y. Tokura, Nature 395 (1998) 677.

[3] M. Fiebig, K. Miyano, Y. Tomioka, Y. Tokura, Science 280 (1998) 1925.
[4] M. Yashima, M. Itoh, Y. Inaguma, Y. Morii, J. Am. Chem. Soc. 127 (2005) 3491.
[5] C.Y. Park, F.V. Azzarello, A.J. Jacobson, J. Mater. Chem. 16 (2006) 3624.
[6] E.J. Cussen, M.J. Rosseinsky, P.D. Battle, J.C. Burley, L.E. Spring, J.F. Vente, S.J. Blundell, A.I. Coldea, J. Singleton, J. Am. Chem. Soc. 123 (2001) 1111.
[7] B. Bakowski, P.D. Battle, E.J. Cussen, L.D. Noailles, M.J. Rosseinsky, A.I. Coldea, J. Singleton, Chem. Commun. (1999) 2209.
[8] J.B. MacChesney, R.C. Sherwood, J.F. Potter, J. Chem. Phys. 43 (1965) 1907.
[9] L.H. Brixner, J. Inorg. Nucl. Chem. 15 (1960) 356.
[10] E.J. Cussen, D.R. Lynham, J. Rogers, Chem. Mater. 18 (2006) 2855.
[11] C.D. Brandle, H. Steinfink, Inorg. Chem. 10 (1971) 922.
[12] A.C. Mclaughlin, Solid State Commun. 137 (2006) 354.
[13] A. Harrison, J. Phys. Condes. Matter 16 (2004) S553.
[14] C.N.R. Rao, R. Mahesh, Curr. Opin. Solid State Mater. Sci. 2 (1997) 32.
[15] H.M. Rietveld, Acta Cryst. 2 (1969) 65.
[16] A.C. Larson, R.B. von Dreele, General Structure Analysis System (GSAS), Los Alamos National Laboratories, 1990.
[17] P.J. Brown, in: International Tables for Crystallography, fourth ed., vol. C, Kluwer Academic Publishers, Dordrecht, 1995, p. 512.
[18] C.J. Howard, B.J. Kennedy, P.M. Woodward, Acta Cryst. B 59 (2003) 463.
[19] C. Ritter, M.R. Ibarra, L. Morellon, J. Blasco, J. Garcia, J.M. De Teresa, J. Phys. Condens. Matter 12 (2000) 8295.
[20] T.S. Chan, R.S. Liu, G.Y. Guo, S.F. Hu, J.G. Lin, J.M. Chen, J.P. Attfield, Chem. Mater. 15 (2003) 425.
[21] N.G. Parkinson, P.D. Hatton, J.A.K. Howard, S.R. Giblin, I. Terry, C. Ritter, B.H. Mok, M.K. Wu, J. Mater. Chem. 15 (2005) 1375.
[22] P.D. Battle, C.W. Jones, F. Studer, J. Solid State Chem. 90 (1991) 302.
[23] N.G. Parkinson, P.D. Hatton, J.A.K. Howard, C. Ritter, R.M. Ibberson, M.-K. Wu, J. Phys. Condens. Matter 16 (2004) 7611.